Scripta Materialia 213 (2022) 114630

Contents lists available at ScienceDirect

Scripta Materialia

journal homepage: www.journals.elsevier.com/scripta-materialia

Effective strengthening and toughening in high entropy-alloy by combining extrusion machining and heat treatment

Zhuo Pu [a], Song-Lin Cai [e], Lan-Hong Dai [b,c,d,*]

[a] Science and Technology on Reactor System Design Technology Laboratory, Nuclear Power Institute of China, Chengdu 610200, China
[b] State Key Laboratory of Explosion Science and Technology, Beijing Institute of Technology, Beijing, 100081, China
[c] State Key Laboratory of Nonlinear Mechanics, Institute of Mechanics, Chinese Academy of Sciences, Beijing 100190, China
[d] School of Engineering Science, University of Chinese Academy of Sciences, Beijing 100049, China
[e] China Electric Power Research Institute, State Grid Corporation of China, Beijing 100192, China

ARTICLE INFO

Keywords:
High-entropy alloy
Extrusion machining
Heat treatment
Strain hardening
Recrystallization

ABSTRACT

This study presents an effective strengthening and toughening approach to improve tensile properties of CrMnFeCoNi high entropy-alloy (HEA) by combining extrusion machining and short-time heat treatment. After such process, preliminary structural heterogeneity has been achieved in this alloy, of which the strength is significantly enhanced while good elongation is retained compared to its homogeneous conterparts. Microstructural characterization reveals varying degrees of partial recrystallization with more or less dislocation density for HEAs under different treatment. It is such structural inhomogeneity that imparts this alloy with good strain hardening ability at high flow stress levels.

Breaking the routine of alloy design, researchers have recently developed high-entropy alloys (HEAs) or complex concentrated alloys (CCAs) that contain multiple elements in equal or near-equal ratios, drawing considerable research attentions over the last decade [1–6]. Owning to their unique chemical complexity caused by random distribution of elements in lattice, HEAs display extraordinary mechanical properties, including superior cryogenic fracture toughness [7,8], excellent performance at high temperatures [9,10], good mechanical behavior under dynamical loading [11–13], and strong damage tolerance [14,15]. Among all kinds of HEAs, the groupings with CoCrNi elements have become the largest branch in the HEA family tree [6] and show significant potential to overcome traditional strength-ductility trade-off [7,14].

As has been summarized, the critical challenge of enhancing ductility in ultra-strong alloys mainly comes from imparting them with sufficiently high rate of strain hardening [16,17]. To better solve such a problem in HEAs, some attempts at composition design have been made by researchers. Switching from the classical equiatomic CrMnFeCoNi 'cantor alloy' [1], the non-equiatomic dual-phase $Fe_{80-x}Mn_xCo_{10}Cr_{10}$ (at%) HEA system with pronounced transformation-induced plasticity (TWIP) effect has been developed, which is proved to have excellent strength-ductility combination [18]. Utilizing the precipitation strengthening strategy, strength and ductility can be substantially improved in a TiZrHfNb refractory HEA by doping ordered oxygen complexes [20]. Moreover, only through the control of microstructures like creating a multi-modal grain size distribution or a mixture of multi-phases with varying size scales and properties [17], strength-ductility combination can also be achieved without changing the composition of the materials. Controllably introducing gradient nano-scaled dislocation-cell structures in a stable single phase $Al_{0.1}$CoCrFeNi HEA, the strength of which is enhanced without apparent ductility loss [19]. Through different combinations of annealing and cooling treatment, heterogeneous structure with grain sizes spanning from nanometers to micrometers has been achieved in a CrCoNi medium-entropy alloy, the strength of which is dramatically enhanced while retaining good ductility [21,22]. By properly mixing the face-centered cubic (FCC) phase and the ordered body-centered cubic (BCC) lamellae, along with its precipitates, a sequentially-activated multistage strain hardening effect is introduced in a $Fe_{20}Co_{20}Ni_{41}Al_{19}$ (at%) eutectic HEA that shows strong abilities in matching high level of strength and ductility [23]. All these above ideas in overcoming strength-ductility trade-off, generally speaking, are derived from a synergistic effect triggered by the interaction of heterogeneous zones in materials with mechanical or phisical variations, and unattainable by their homogeneous counterparts [24].

A classic method of inhomogenization in materials is to refine the

* Corresponding author at: State Key Laboratory of Nonlinear Mechanics, Institute of Mechanics, Chinese Academy of Sciences, Beijing 100190, China.
E-mail address: lhdai@lnm.imech.ac.cn (L.-H. Dai).

https://doi.org/10.1016/j.scriptamat.2022.114630
Received 8 January 2022; Received in revised form 13 February 2022; Accepted 21 February 2022
Available online 2 March 2022

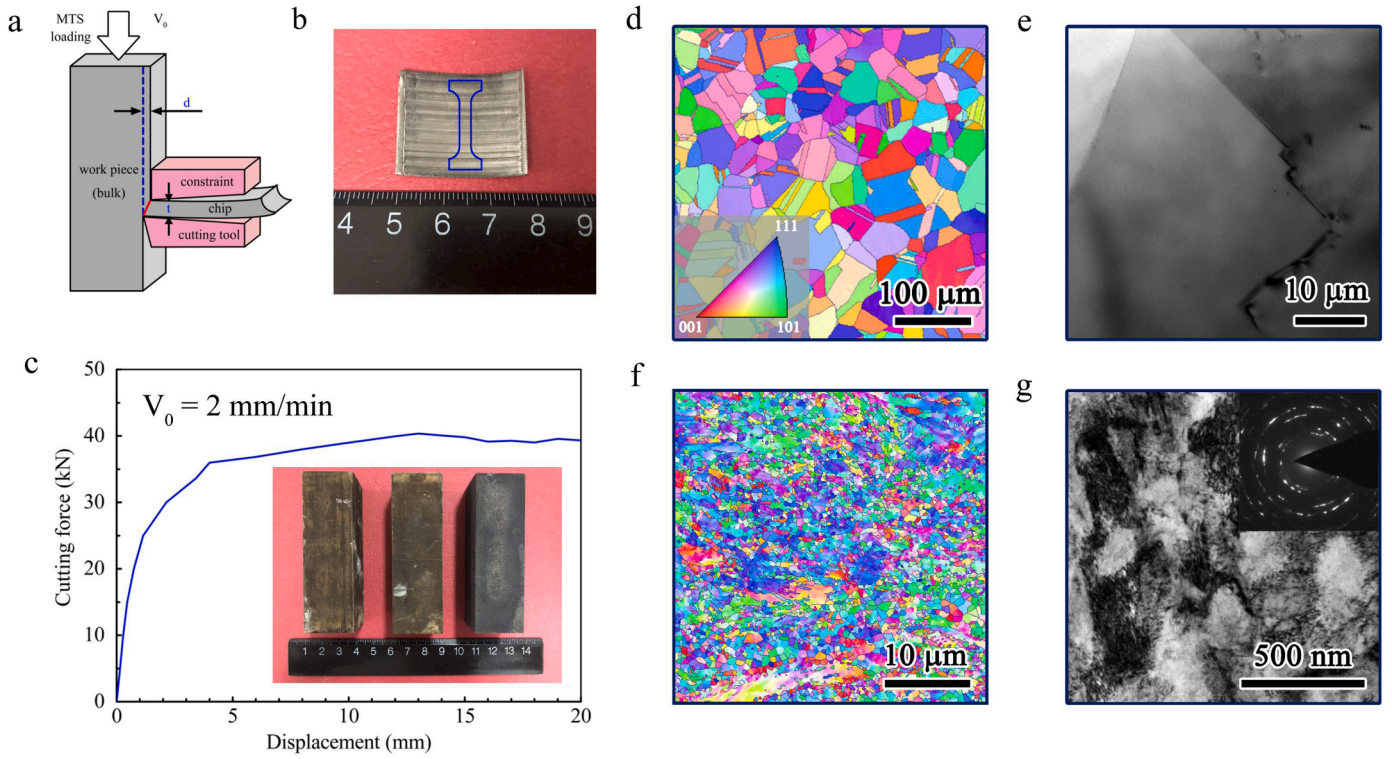

Fig. 1. (a) Schematic diagram of experimental equipment for QSEM; (b) a HEA chip after QSEM and the sampling method of tensile specimen; (c) experimental measurements of cutting forces in QSEM, and the inset shows the initial HEA workpieces; (d, e) and (f, g) are the micristructures of the HEA before and after QSEM, respectively.

grains by severe plastic deformation (SPD) [25–27], and partially recrystallize the refined grains by subsequent heat treatment, as has been done in nanostructured or ultrafine-grained copper [28,29]. Compared with conventional developed SPD methods, e.g. equal channel angular extrusion or high pressure torsion, large strain machining stands out as a relatively new technique that ensures metallic materials to achieve SPD in a single pass [29–31]. In this study, ultrafine-grained cantor alloy was obtained using a quasi-static extrusion machining (QSEM) [29]. Followed by short-time heat treatment under different conditions, partial recrystallization has been produced, resulting in structural inhomogeneity in such alloy. Tensile tests show that, the strength of the inhomogeneous specimens is substantially higher than its homogeneous counterparts while good ductility is retained. Microstructural characterizations were further conducted to reveal the differences in plastic deformation details between this alloy with partial and full recrystallization.

The equimolar CrMnFeCoNi HEA was produced by arc-melting a mixture of pure metals with a nominal composition $Cr_{20}Mn_{20}Fe_{20}Co_{20}Ni_{20}$ (at%) in a high purity argon atmosphere. To ensure chemical homogeneity, the ingots were remelted at least five times before the drop-cast process. The as-cast ingots were subsequently hot forged at 1373 K to sheets having a final thickness of ~3 cm, followed by homogenizing annealing at 1373 K for 1 h and electric discharge machining, the initial HEA workpieces with dimensions of 25 × 25 × 80 mm^3 was obtained, as shown by the inset in Fig. 1c.

The initial HEA workpieces were processed by means of QSEM at room temperature using a MTS-CMT5105S (Fig. 1a). The tool with a precut thickness d is cutting the workpiece at cutting speed V_0, while the chip thickness t is controlled by the constraint (See refs [29,32] for more experimental details about QSEM). In consideration of the expansion effect of the chip during free machining [32], along with achieving sufficient SPD of materials, values of the above parameters are chosen to be d = 0.2 mm, t = 0.6 mm and V_0 = 2 mm/min, respectively, after different attempts. The red line extends from the constraint to the cutting tool in Fig. 1a represents the primary shear zone (PSZ) [33], approaching which the shear stress and strain in material builds up rapidly. Ignoring the extrusion effect, a simple estimation of shear strain, γ, in PSZ is given by De Chiffre [34]:

$$\gamma = \frac{\lambda}{cos(\alpha)} + \frac{1}{\lambda \cos(\alpha)} - 2tan(\alpha), \quad (1)$$

where $\lambda = d/t$ is the chip thickness ratio and α is the tool rake angle. Adopting λ to be ~0.67 and α to be ~ 10° [32] in Eq. (1), γ is estimated to be ~1.84 for the HEA in this study. Besides, Fig. 1c presents the cutting force-displacement curves, where the cutting force eventually fluctuates around 4 kN. Fig. 1b shows a HEA chip after QSEM under the condition abovementioned.

After QSEM, the HEA chips were annealed at 973 K for 5 min (sample *A*), 10 min (sample *B*) and 15 min (sample *C*), and 1073 K for 5 min (sample *D*) to introduce varying degrees of partial recrystallization. After these heat treatment, specimens for uniaxial tensile tests were cut from the annealed chips and the sampling method is denoted by the blue line in Fig. 1b. Quasi-static uniaxial tensile tests were carried out on the MTS-CMT5105S with a strain rate of 10^{-3} s^{-1}. Thin foils with a diameter of 3 mm were punched out from the gauge section of HEA samples before and after tensile tests. Using a twin jet polish system, the electron transparent regions were prepared to further characterize the microstructures using transmission electron microscope (TEM, JEOL, JEM-2100F).

Representative microstructures of the HEA before and after QSEM are exhibited in Fig. 1d–g. Inverse pole figure (IPF) of the initial HEA workpiece shows an equiaxed grain structure with an average grain size of ~50 μm (Fig. 1d), observed using electron backscatter diffraction (EBSD) imaging. Besides, numerous annealing twins have been formed in this alloy due to homogenizing heat treatment. A typical region with distinct grain boundaries displays low dislocation density, as shown by the TEM micrograph in Fig. 1e. With regard to the HEA chip after QSEM,

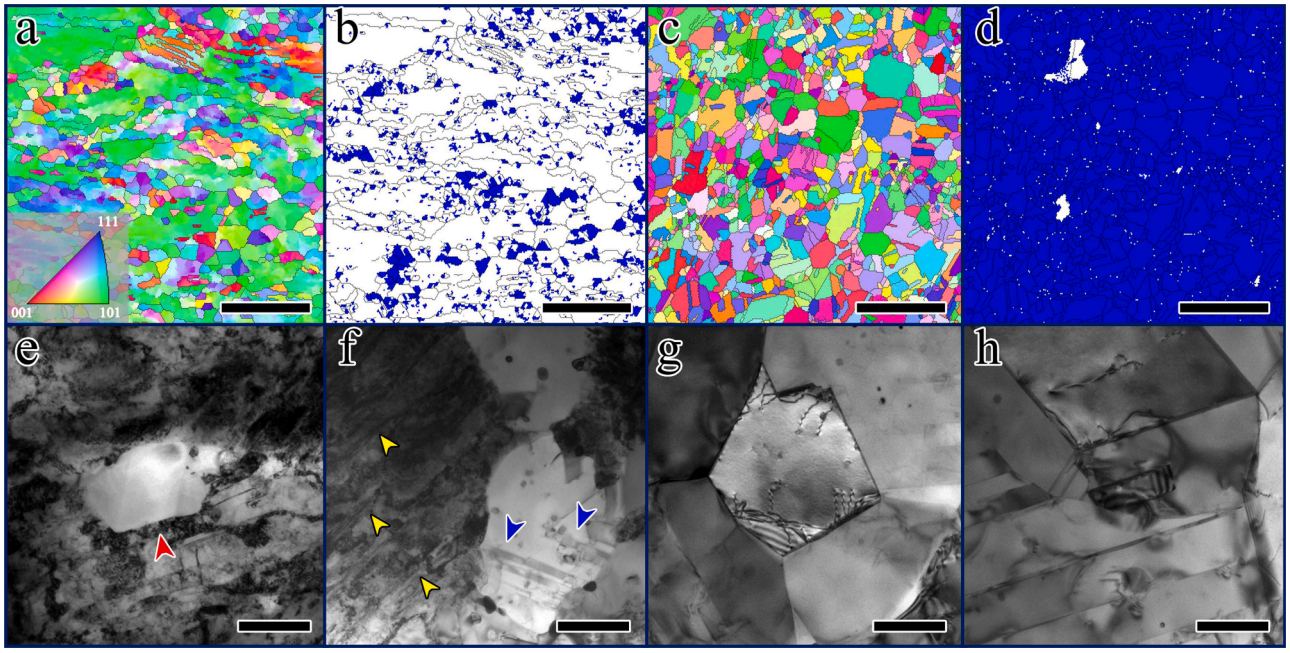

Fig. 2. (a) and (b) are IPF and GROD map for sample *A*, respectively; (c) and (d) are IPF and GROD map for sample *D*, respectively; (e,f) and (g,h) are representative TEM micrographs of sample *A* and sample *D*, respectively. The scale bars in (a-d) are 10 μm, and the scale bars in (g-h) are 500 nm.

the IPF indicates that a remarkable grain refinement phenomenon has occurred (Fig. 1f), where the average grain size has been reduced to ~1 μm, a threshold for achieving ultrafine-grained alloys. The corresponding TEM micrograph is shown in Fig. 1g, which further reveals the details of these refined grains with dramatically enhanced dislocation density. The inset in Fig. 1g is the corresponding selected area diffraction (SAD) patterns indicating typical polycrystalline diffraction characterization lack of strong texture.

Fig. 2 a presents the IPF of sample *A*, where the grains have slightly grown compared to the HEA chip with only QSEM treatment. A heterogeneous distribution of grain sizes ranging from ~1 μm to ~10 μm has emerged in this sample due to annealing at 973 K for 5 min. The grain reference orientation deviation (GROD) map [35] of sample *A* is shown by Fig. 2b, where the blue regions are considered to be the recrystallized grains with intragranular misorientation $< 1^{\circ}$ [22]. Compared with sample *A*, sample *D* shows a more uniform grain distribution and a certain amount of annealing twins (see Fig. 2c), as a result of annealing at higher temperature (1073 K) for the same time. Meanwhile, the corresponding GROD map of sample *D* reveals a much more fully developed recrystallization phenomenon than that in sample *A*, as shown in Fig. 2d. Further, the representative TEM micrographs of sample *A* are displayed by Fig. 2e,f. An almost dislocation-free recrystallized grain (denoted by the red arrow) with a size of ~500 nm was found, surrounded by a large number of refined grains with high dislocation density (Fig. 2e). Moreover, the recrystallized grain observed in Fig. 2f contains several thin annealing twins, as marked by the blue arrows. The left area of Fig. 2f shows large amount of residual dense dislocation walls (DDWs, marked by the yellow arrows) [36–38] which are the result of QSEM. These inhomogeneous microstructures of sample *A* indicate that the preliminary structural inhomogeneity of HEA has been achieved by combining QSEM and short-time heat treatment. On the other hand, the more homogeneous microstructures of sample *D* induced by relatively fully recrystallization have been revealed by TEM images shown in Fig. 2g,h. The previously refined grains after QSEM are almost unobservable and replaced by a large number of recrystallized grains with more distinct grain boundaries than those in sample *A* (Fig. 2g). More and thicker annealing twins can also be observed in Fig. 2h. The large structural difference between sample *A* and *D* implies that this alloy is sensitive to annealing temperature after QSEM.

Tensile engineering stress-strain ($\sigma - \varepsilon$) curves for initial workpieces, chips after QSEM, and samples $A - D$ are displayed in Fig. 3a. Compared with the initial workpiece that has a yield strength, σ_y, of ~400 MPa and a uniform elongation, ε_u, of ~0.39 (marked by the small square), σ_y of the HEA chips after QSEM has been significantly increased to ~1.4 GPa however, almost all the plastic elongation is sacrificed. This indicates that the QSEMed chips with ultrafined grains and a high dislocation density have almost no work hardening ability. After annealing at 973 K for 5 min, ε_u of sample *A* was raised to ~0.11 while σ_y of this sample can be maintained at ~950 MPa (see curve *A*), compared to the chips with only the QSEM treatment. Hence, through such a short-time heat treatment after QSEM, this alloy has obtained a good strain hardening ability at the stress level of close to 1 GPa. Besides, for QSEMed chips that have been heat treated for longer times or at a higher temperature (samples $B - D$), ε_u is further improved, with a further decrease in σ_y. Nevertheless, compared with the initial workpiece, σ_y of sample *D* was increased by 200 MPa and ε_u remained almost the same. It is interesting to note a better tensile behaviors of samples $A - D$ than the initial workpieces or several cantor alloys with other treatment (see the data points in the yellow area in Fig. 3d), suggesting strong potential of combining such QSEM technique and short-time heat treatment to improve the ability of HEA to match strength and ductility if better processing parameters can be selected. Fig. 3b and 3 c is the corresponding true stress-strain and strain hardening rate curves of Fig. 3a, respectively. After yield, the strain hardening rate, Θ, of sample *A* decreases monotonically with strain, while an upturn [21] of Θ has occurred in samples $B - D$, as shown by the inset in Fig. 3c. This is mainly attributed to the difference in initial dislocation density between sample *A* and samples $B - D$ after yield, which results in different work hardening behaviors at early strain stages [39].

Fig. 4 a–e provides TEM micrographs of sample *A* after fracture. In most regions, the microstructures of this sample are elongated grains with high dislocation density, as shown by Fig. 4a,b. The initial recrystallized grains with few dislocations are barely visible because during plastic deformation, these softer recrystallized grains preferentially accommodate strains, producing dislocations and structures like twin boundaries and subgrain boundaries [28], which in turn refine such recrystallized grains. Fig. 4c,d shows pronounced deformation-induced

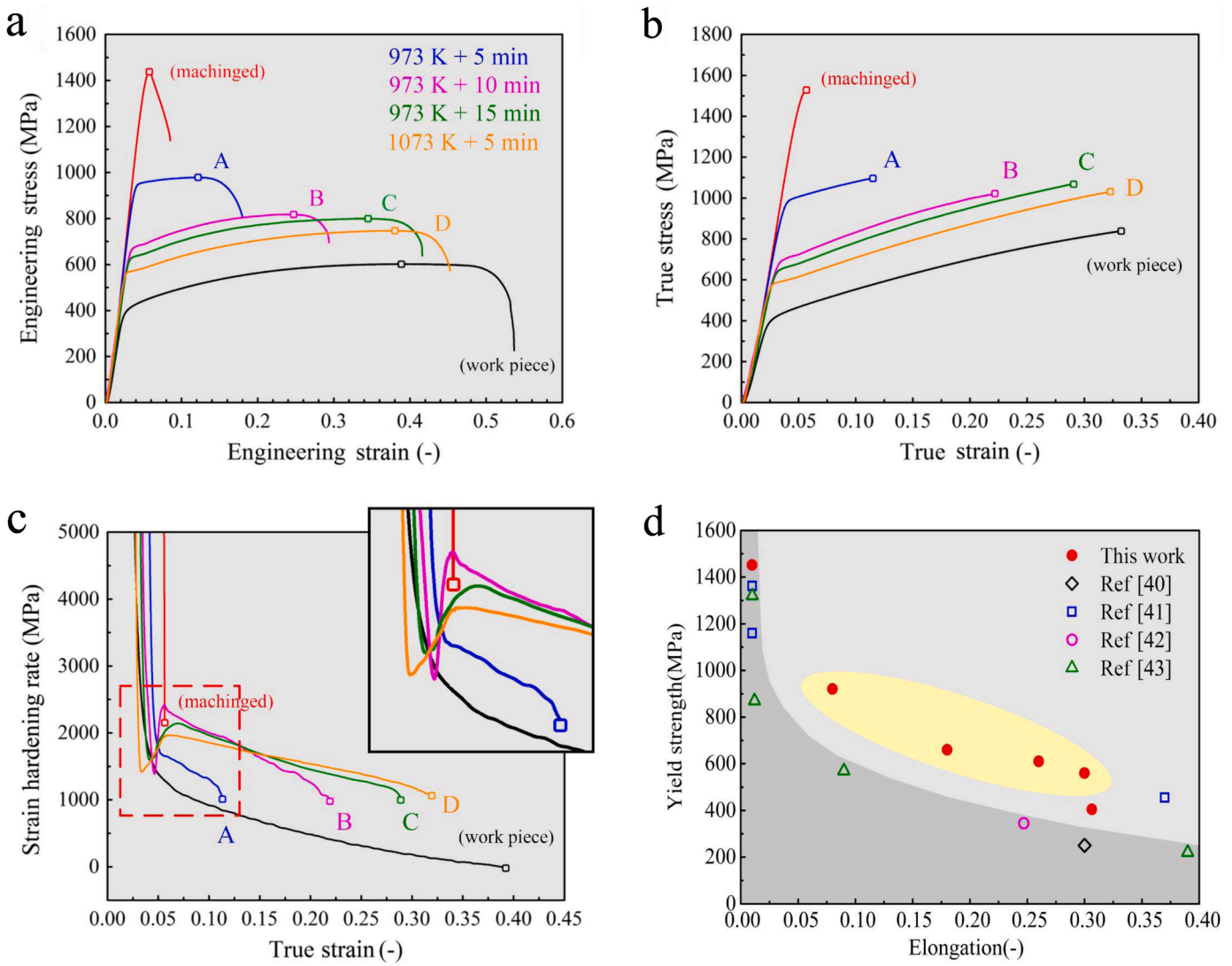

Fig. 3. (a) Engineering stress-strain curves for initial workpiece, chip after QSEM and samples $A-D$. (b) and (c) are true stress-strain curves and the corresponding work hardening rates for all the samples described above, respectively. (d) Yield stress vs. uniform elongation for the present HEA, along with the data for cantor alloy with different heat treatment (The data in this figure are true stress and true strain).

twinning (denoted by the red arrows), as an additional plastic deformation mode besides slip, it enhances the work hardening ability by introducing extra interfaces [8]. Here, we emphasize that such twins were mainly produced by tensile deformation in the recrystallized regions rather than by QSEM in the non-recrystallized regions, since the twins produced during QSEM, if any, would be likely to annihilate as a result of de-twining process at large strain stages [40–42], and finally only refined grains could be observed (see Fig. 1g). Interestingly, a certain number of annealing twins with relatively lower dislocation densities were still observed, of which the twin boundaries were marked by the blue arrows, as displayed in Fig. 4e. Since de-twinning phenomenon can also lead the annealing twins to disappear, these residual annealing twins imply that plastic deformation of the recrystallized regions of sample *A* is not so uniform. For the sake of comparison, the microstructure characterization of sample *D* was also conducted, as shown by Fig. 4f–i. Different from sample *A*, tangled dislocations occupy most regions of sample *D* (Fig. 4f–h) and the morphologies of grains are not significantly elongated. These differences mainly come from the different grain size distributions and dislocation densities between the initial state of the two samples. Moreover, only a few bundles of deformation twins were observed in sample *D* (denoted by the yellow arrows in Fig. 4i), of which the reason can be attributed to its smaller flow stress compared to sample *A*. According to systematic tensile experiments with varying degrees of strain stage [43], deformation twinning starts after a "critical" true stress (720 ± 30 MPa) in a polycrystalline cantor alloy with a mean grain size of ~17 μm, and the volume fraction of twins was found to increase with the rise of flow stress. Therefore, in this study, the difference in average flow stress between sample *A* and sample *D* (see Fig. 3b) is considered to be one of the dominating factors causing the variance in their number of deformation twins.

Utilizing QSEM and short-time heat treatment, preliminary structural heterogeneity has been achieved in classical cantor alloy. Microstructure observations indicate that the heterogeneous structures are mainly consisted of varying degrees of partial recrystallized grains with different dislocation densities. Compared with the initial workpieces, strength of samples $A-D$ has been greatly improved while good elongation can be retained. Deformation microstructure characterizations suggest that elongated grains and deformation twins impart sample *A* with yield stress of ~950 MPa a good strain hardening ability. These results provide evidence supporting the effectiveness of combining extrusion machining and heat treatment in overcoming the strength-ductility paradox in HEAs.

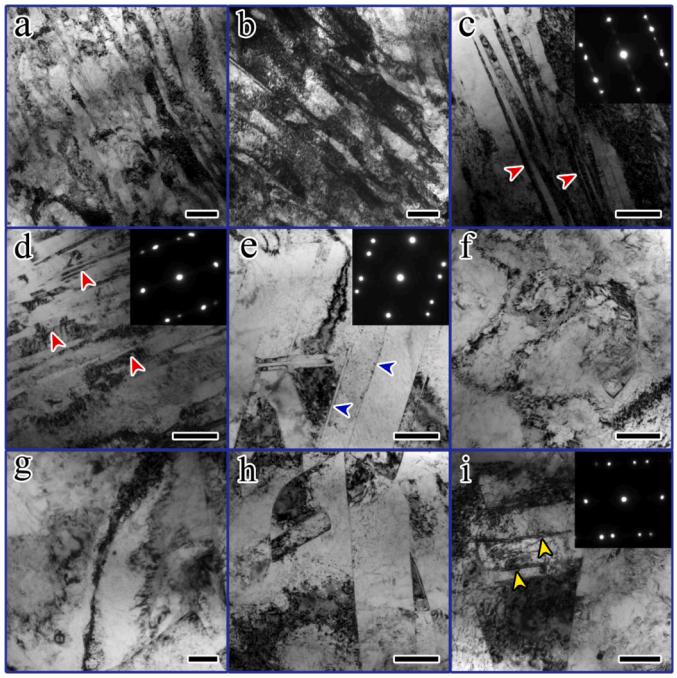

Fig. 4. TEM micrographs of (a–e) sample *A* and (f,i) sample *D* after fracture. The insets in (c–e) and (i) are the corresponding SAD patterns. All the scale bars are 200 nm.

Declaration of Competing Interest

The authors declare that they have no known competing financial interests or personal relationships that could have appeared to influence the work reported in this paper.

Acknowledgment

This research was supported by the NSFC Basic Science Center Program for "Multiscale Problems in Nonlinear Mechanics" (Grant No. 11988102), the NSFC (No. 11790292), Ye Qisun Science Foundation of National Science Foundation of China (U2141204), the Strategic Priority Research Program of the Chinese Academy of Sciences (Nos. XDB22040302 and XDB22040303), the Key Research Program of Frontier Sciences of the Chinese Academy of Sciences (No. QYZDJSSW-JSC011).

References

[1] B. Cantor, I.T.H. Chang, P. Knight, A.J.B. Vincent, Mater. Sci. Eng. A 375–377 (2004) 213–218.
[2] J.W. Yeh, S.K. Chen, S.J. Lin, J.Y. Gan, T.S. Chin, T.T. Shun, C.H. Tsau, S.Y. Chang, Adv. Eng. Mater. 6 (2004) 299–303.
[3] Y. Zhang, T.T. Zuo, Z. Tang, Z. Tang, M.C. Gao, K.A. Dahmen, P.K. Liaw, Z.P. Lu, Prog. Mater. Sci. 61 (2014) 1–93.
[4] Z.Z. Li, S.T. Zhao, R.O. Ritchie, M.A. Meyers, Prog. Mater. Sci. 102 (2019) 296–345.
[5] E.P. George, D. Raabe, R.O. Ritchie, Nat. Rev. Mater. 4 (2019) 515–534.
[6] D.B. Miracle, O.N. Senkov, Acta Mater. 122 (2016) 448–511.
[7] B. Gludovatz, A. Hohenwarter, D. Catoor, E.H. Chang, E.P. George, R.O. Ritchie, Science 345 (2014) 1153–1158.
[8] F. Otto, A. Dlouhý, C. Somsen, H. Bei, G. Eggeler, E.P. George, Acta Mater. 61 (2013) 5743–5755.
[9] O.N. Senkov, G.B. Wilks, J.M. Scott, D.B. Miracle, Intermetallics 19 (2011) 698–706.
[10] Y.M. Huang, Z.Y. Wang, Z.Z. Xu, X.M. Zang, X.G. Chen, Mater. Lett. 285 (2020) 129004.
[11] Z.J. Jiang, J.Y. He, H.Y. Wang, H.S. Zhang, Z.P. Lu, L.H. Dai, Mater. Res. Lett. 4 (2016) 226–232.
[12] Z.Z. Li, S.T. Zhao, S.M. Alotaibi, Y. Liu, B.F. Wang, Acta Mater. 151 (2018) 424–431.
[13] X.F. Liu, Z.L. Tian, X.F. Zhang, H.H. Chen, T.W. Liu, Y. Chen, Y.J. Wang, L.H. Dai, Acta Mater. 186 (2020) 257–266.
[14] Z.J. Zhang, M.M. Mao, J.W. Wang, B. Gludovatz, Z. Zhang, S.X. Mao, E.P. George, Q. Yu, R.O. Ritchie, Nat. Commun. 6 (2015) 10143.
[15] K. Liu, S.S. Nene, M. Frank, S. Sinha, R.S. Mishra, Mater. Res. Lett. 6 (2018) 613–619.
[16] E. Ma, Scr. Mater. 49 (2003) 663–668.
[17] E. Ma, JOM 58 (2006) 49–53.
[18] Z.M. Li, K.G. Pradeep, Y. Deng, D. Raabe, C.C. Tasan, Nature 534 (2016) 227–230.
[19] Q.S. Pan, L.X. Zhang, R. Feng, Q.H. Lu, K. An, A.C. Chuang, J.D. Poplawsky, P. K. Liaw, L. Lu, Science 374 (2021) 984–989.
[20] Z.F. Lei, X.J. Liu, Y. Wu, H. Wang, S.H. Jiang, S.D. Wang, X.D. Hui, Y.D. Wu, B. Gault, P. Kontis, D. Raabe, L. Gu, Q.H. Zhang, H.W. Chen, H.T. Wang, J.B. Liu, K. An, Q.S. Zeng, T. Nieh, Z.P. Lu, Nature 563 (2018) 546–550.
[21] M.X. Yang, D.S. Yan, F.P. Yuan, P. Jiang, E. Ma, X.L. Wu, Proc. Natl. Acad. Sci. 115 (2018) 7224–7229.
[22] C.E. Slone, J. Miao, E.P. George, M.J. Mills, Acta Mater. 165 (2019) 496–507.
[23] P.J. Shi, Y.B. Zhong, Y. Li, W.L. Ren, T.X. Zheng, Z. Shen, B. Yang, J.C. Peng, P. F. Hu, Y. Zhang, P.K. Liaw, Y.T. Zhu, Mater. Today 41 (2020) 62–71.
[24] Y.T. Zhu, K. Ameyama, P.M. Anderson, I.J. Beyerlein, H.J. Gao, H.S. Kim, E. Lavernia, S. Mathaudhu, H. Mughrabi, R.O. Ritchie, N. Tsuji, X.Y. Zhang, X. L. Wu, Mater. Res. Lett. 9 (2021) 1–31.
[25] R.Z. Valiev, R.K. Islamgaliev, I.V. Alexandrov, Prog. Mater. Sci. 45 (2000) 103–189.
[26] Y. Estrin, A. Vinogradov, Acta Mater. 61 (2013) 782–817.
[27] R.Z. Valiev, Y. Estrin, Z.J. Horita, T.G. Langdon, M.J. Zehetbauer, Y.T. Zhu, JOM 58 (2016) 33–39.
[28] Y.M. Wang, M.W. Chen, F.H. Zhou, F.H. Zhou, E. Ma, Nature 419 (2002) 912–915.
[29] Y. Liu, S.L. Cai, F.G. Xu, Y.J. Wang, L.H. Dai, J. Mater. Process. Technol 267 (2019) 52–60.
[30] M. Efe, W. Moscoso, K.P. Trumble, W.D. Compton, S. Chandrasekar, Acta Mater. 60 (2012) 2031–2042.
[31] J.G. Gigax, O. El-Atwani, Q. McCulloch, B. Aytuna, M. Efe, S. Fensin, S.A. Maloy, N. Li, Scr. Mater. 178 (2020) 508–512.
[32] Y. Liu, S.L. Cai, X.C. Shang, L.H. Dai, Nonlinear Dyn. 88 (2017) 433–453.
[33] F. Zeng, M.Q. Jiang, L.H. Dai, Proc. R. Soc. A 474 (2018) 20170836.
[34] L. De Chiffre, Int. J. Mach. Tool Des. Res. 16 (1976) 137–144.
[35] I. Gutierrez-Urrutia, F. Archie, D. Raabe, F.K. Yan, N.R. Tao, K. Lu, Sci. Technol. Adv. Mater. 17 (2016) 29–36.
[36] Q. Liu, N. Hansen, Scr. Metall. Mater. 32 (1995) 1289–1295.
[37] Q. Liu, D.J. Jensen, N. Hansen, Acta Mater. 46 (1998) 5819–5838.
[38] I. Gutierrez-Urrutia, D. Raabe, Acta Mater. 60 (2012) 5791–5802.
[39] A. Seeger, J. Diehl, S. Mader, H. Rebstock, Philos. Mag. 2 (1957) 323–350.
[40] C.S. Hong, N.R. Tao, X. Huang, K. Lu, Acta Mater. 58 (2010) 3103–3116.
[41] J. Wang, N. Li, O. Anderoglu, X. Zhang, A. Misra, J.Y. Huang, J.P. Hirth, Acta Mater. 58 (2010) 2262–2270.
[42] M.J. Szczerba, S. Kopacz, M.S. Szczerba, Acta Mater. 104 (2016) 52–61.
[43] G. Laplanche, A. Kostka, O.M. Horst, G. Eggeler, E.P. George, Acta Mater. 118 (2016) 152–163.